JACS
JOURNAL OF THE AMERICAN CHEMICAL SOCIETY
pubs.acs.org/JACS

Open Access
This article is licensed under CC-BY-NC-ND 4.0

Article

Electrochemical Formation of C_{2+} Products Steered by Bridge-Bonded *CO Confined by *OH Domains

Haibin Ma, Enric Ibáñez-Alé, Futian You, Núria López,* and Boon Siang Yeo*

Cite This: J. Am. Chem. Soc. 2024, 146, 30183−30193

Read Online

ACCESS | Metrics & More | Article Recommendations | Supporting Information

ABSTRACT: During the electrochemical CO_2 reduction reaction (eCO_2RR) on copper catalysts, linear-bonded CO ($*CO_L$) is commonly regarded as the key intermediate for the CO-CO coupling step, which leads to the formation of multicarbon products. In this work, we unveil the significant role of bridge-bonded *CO ($*CO_B$) as an active species. By combining *in situ* Raman spectroscopy, gas and liquid chromatography, and density functional theory (DFT) simulations, we show that adsorbed *OH domains displace $*CO_L$ to $*CO_B$. The electroreduction of a $^{12}CO + ^{13}CO_2$ cofeed demonstrates that $*CO_B$ distinctly favors the production of acetate and 1-propanol, while $*CO_L$ favors ethylene and ethanol formation. This work enhances our understanding of the mechanistic intricacies of $eCO_{(2)}RR$ and suggests new directions for designing operational conditions by modifying the competitive adsorption of surface species, thereby steering the reaction toward specific multicarbon products.

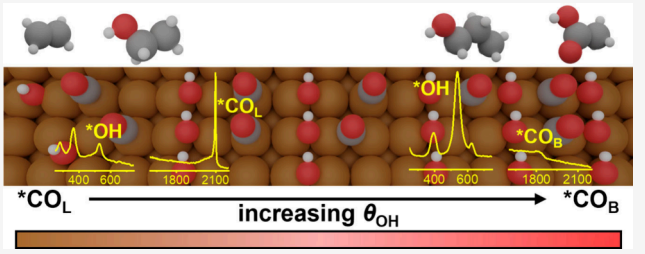

INTRODUCTION

The electrochemical CO_2 reduction reaction (eCO_2RR) to multicarbon products on copper-based catalysts has emerged as a promising approach for recycling carbon and thus reducing our reliance on fossil fuels.[1] This process involves primarily the electroconversion of CO_2 into adsorbed *CO.[2] The *CO intermediate then participates in CO-CO coupling, which is generally accepted to be the rate-determining step toward the formation of more complex products such as ethylene, acetate, 1-propanol, etc. The adsorption configuration of *CO and the presence of other coadsorbates can thus significantly impact the efficiency of eCO_2RR, since the rate for subsequent reactions can be altered by the electronic and geometric interactions between the *CO and the catalytic environment.

CO produced from eCO_2RR mainly binds on Cu surfaces in a linear configuration ($*CO_L$), exhibiting a broad C≡O stretching band ($\nu_{C\equiv O}$) centered between 2000 and 2100 cm^{-1}.[3−5] Some works have deconvoluted this broad band and assigned it to $*CO_L$ bonded on Cu sites with different coordination numbers.[4,5] Weckhuysen and co-workers further proposed that $*CO_L$ with a high $\nu_{C\equiv O}$ frequency (∼2090 cm^{-1}) tends to desorb directly, while $*CO_L$ with a low frequency (∼2060 cm^{-1}) tends to undergo coupling, forming C_{2+} products like ethylene.[6]

While many works have reported that the $*CO_L$ species is active for CO-CO coupling, resulting in $*CO_L$ frequently serving as the basis for computational models, others have shown that *CO can adopt a bridge adsorption configuration ($*CO_B$) under specific conditions during eCO_2RR.[7−9] For instance, both $*CO_L$ and $*CO_B$ species were identified during eCO_2RR on an amine-terminal, dendrimer-functionalized Cu catalyst, on which acetate was formed with a high Faradaic efficiency (FE) of 47%.[10] Acetate and propanol selectivity has also been promoted on Cu by controlling CO partial pressure during eCO_2RR, where $*CO_B$ was observed.[11]

$*CO_B$ can be further detected when CO is directly supplied as a feedstock.[12] An *in situ* infrared spectroscopy study has shown that during eCORR, $*CO_B$ ($\nu_{C\equiv O}$ =∼ 1865 cm^{-1}) became the dominant species for prolonged periods from −0.1 to −1.5 V_{SCE} (SCE: saturated calomel electrode).[13] Liu et al. have suggested that directly supplied CO can reconstruct the Cu surface, which favors the formation of $*CO_B$.[14] Some works have proposed that the $*CO_B$ are inactive, as their signal intensities do not appear to decrease under negative potentials.[15,16] Xu and co-workers have further observed that during eCORR, when the electrolyte was changed from $KHCO_3$ to K_2CO_3, and then to KOH, the CO adsorption configuration completely shifted from linear to bridge.[17,18] Here, we note that even when the aforementioned Cu catalyst was completely covered by supposedly inactive $*CO_B$, it exhibited high C_2 selectivity. Specifically, a 9% FE for C_{2+} products was found on this $*CO_B$-covered surface. In comparison, the FE for C_{2+} products was only 1.6% at the

Received: June 28, 2024
Revised: October 18, 2024
Accepted: October 21, 2024
Published: October 29, 2024

Downloaded via 193.147.222.243 on December 11, 2024 at 19:29:14 (UTC).
See https://pubs.acs.org/sharingguidelines for options on how to legitimately share published articles.

© 2024 The Authors. Published by American Chemical Society

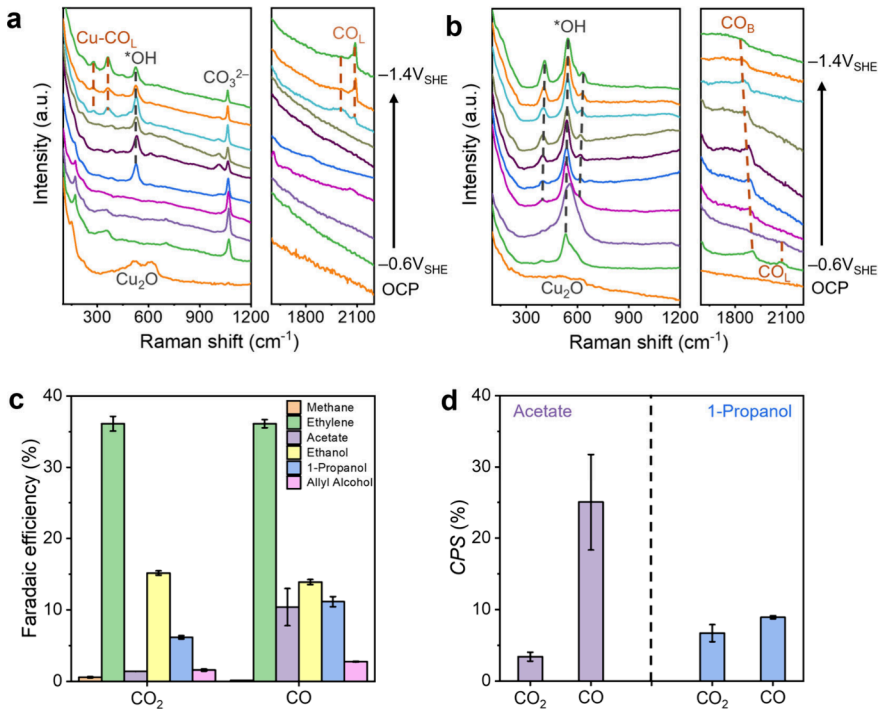

Figure 1. (a,b) Normalized Raman spectra obtained during (a) eCO_2RR and (b) eCORR on a Cu GDE mounted in a flow cell at OCP (open circuit potential) and from −0.6 to −1.4 V_{SHE}. Spectra were collected at potential intervals of 0.1 V. (c) Faradaic efficiencies of major eCO_2RR and eCORR products and (d) *CO-related product selectivity (CPS) of acetate and 1-propanol on a Cu GDE at −1.4 V_{SHE}. All measurements were performed in 1 M KOH (pH 14) electrolyte.

same potential (vs standard hydrogen electrode (SHE)) when the surface was covered by $*CO_L$.[18]

While numerous spectroscopic studies have investigated the nature of *CO on Cu surfaces and its impact on reactivity, these are based on Cu disks placed in traditional H-cells, which are known for their low CO_2 mass transfer.[19,20] Consequently, the results obtained may not be directly relatable to reactivity data from flow cells, which are increasingly considered for industrial-scale eCO_2RR. In this work, we employ a combination of *in situ* Raman spectroscopy, product analyses, and deuterium- and ^{13}C- isotope labeling experiments on Cu-based gas diffusion electrodes (GDE) mounted in H-cells and flow cells. Our approach allows us to unveil the factors influencing the binding configuration of *CO species and, consequently, their reactivity to specific C_{2+} products during eCO_2RR. The presence of Cu-OH species was found to correlate with the shifting of $*CO_L$ to $*CO_B$, and with the changes in the product selectivity from ethylene and ethanol to acetate and 1-propanol. Density functional theory (DFT) simulations elucidate how the arrangement of *OH at high coverage forms stripe-structures that break regular $*CO_L$ domains, thereby generating local $*CO_B$ domains with a lower CO-CO coupling barrier, which are more likely to produce acetate and 1-propanol. This work enhances our understanding of the features affecting the *CO adsorption configuration and its reactivity, paving the way for a more rational design of Cu catalysts and optimization of the conditions for eCO_2RR.

RESULTS AND DISCUSSION

Comparison of CO_2R and COR in Flow Cells. We begin with *in situ* Raman spectroscopic- and product-analyses of eCO_2RR and eCORR (Figures S1−S3). Constant-potential electrolysis was conducted on a Cu GDE in 1 M KOH electrolyte using a homemade Raman flow cell. The same type of Cu GDE was used to collect data throughout this work so that the results could be better compared. All Raman spectra were normalized to the low-frequency background at 100 cm^{-1} (from the silica optics) to compensate for differences in signal intensities due to varying laser focus.[21] The results for eCO_2RR are shown in Figure 1a. At the open circuit potential (OCP), bands at 516 and 614 cm^{-1} were observed. These features can be assigned to a native overlayer of Cu_2O (Table S1).[22] These bands diminished rapidly upon electrode polarization from −0.6 to −1.4 V_{SHE}. All potentials cited hereafter are referenced to the SHE since the formation of C_{2+} products is independent of pH.[23−26] At −0.9 V_{SHE}, a band at ∼525 cm^{-1} appeared. This signal is typically attributed to Cu-OH species.[21,27,28] At −1.2 V_{SHE}, two bands centered at 2011 and 2086 cm^{-1} emerged, which can be attributed to the $*CO_L$ bonded on Cu surface with different coordination numbers, in line with previous reports.[3,4] Two bands at 278 and 361 cm^{-1}, corresponding respectively to the frustrated rotation and stretching of Cu-$*CO_L$, also become apparent.[29] Additionally, a band at 1065 cm^{-1} can be observed. This signal is due to the formation of CO_3^{2-} by the reaction of CO_2 with OH^- in the electrolyte.[27,30]

In contrast, when CO was utilized as feedstock, Cu-OH species appeared immediately upon applying an electrode potential of −0.6 V_{SHE}, as indicated by its signal at 530 cm^{-1} (Figure 1b).[21,27,28] As the bias changed from −0.6 to −1.4 V_{SHE}, the Cu-OH species evolved to give three distinct bands at 399, 540, and 626 cm^{-1} (at −1.4 V_{SHE}) with the band at 540 cm^{-1} exhibiting the strongest intensity. H/D isotopic substitution experiments showed that these bands shifted to 389, 533, and 617 cm^{-1} (at −1.4 V_{SHE}), further indicating that they belong to Cu-OH (Figure S4). The Cu-OH band

https://doi.org/10.1021/jacs.4c08755
J. Am. Chem. Soc. 2024, 146, 30183−30193

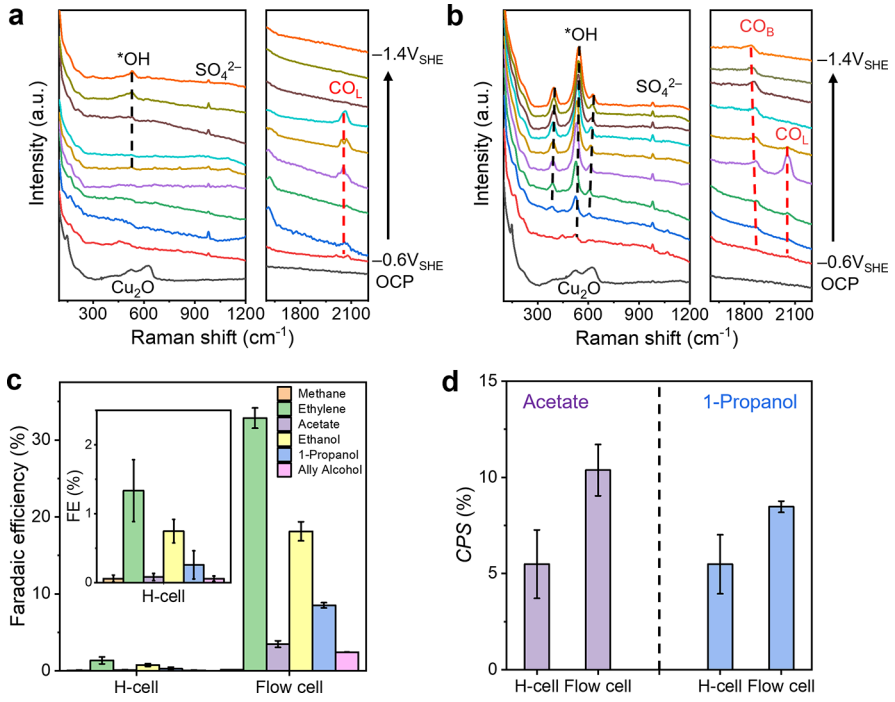

Figure 2. (a,b) Normalized Raman spectra obtained for eCORR on a Cu GDE mounted in (a) H-cell and (b) flow cell at OCP and from −0.6 to −1.4 V_{SHE} in 0.5 M K_2SO_4 (pH 7) electrolyte. Spectra were acquired at potential intervals of 0.1 V. (c) Faradaic efficiency of major eCORR products (insert: enlarged part of the FEs in H-cell) and (d) CPS of acetate and 1-propanol formed on a Cu GDE in H-cell and flow cell at −1.4 V_{SHE} in 0.5 M K_2SO_4 electrolyte.

exhibited a lower intensity during eCO_2RR, as compared to eCORR. This is likely due to the acidic CO_2 consuming the OH^- in the electrolyte to form carbonate and H^+, which lowers the local pH and suppresses the formation of Cu-OH.[18,31] CO also adsorbed on the Cu surface immediately upon application of an electrode potential. However, unlike eCO_2RR which yielded $*CO_L$, directly supplied CO adsorbs differently. At a relatively positive potential of −0.6 V_{SHE}, CO adsorbed as both a linear ($\nu_{C\equiv O}$ = 2072 cm^{-1}) and bridge ($\nu_{C\equiv O}$ = 1901 cm^{-1}) species. The signals of these two *CO species decrease after the potential shifts to −0.7 V_{SHE}. This might result from a disordered layer of Cu-OH formed at this potential, which blocks the CO adsorption sites (Figure S5). As the potential shifts from −0.8 to −1.4 V_{SHE}, the signal from $*CO_L$ at 2072 cm^{-1} disappeared, leaving behind $*CO_B$ with a $\nu_{C\equiv O}$ band of 1826−1901 cm^{-1}. It is noteworthy that the shift from $*CO_L$ to $*CO_B$ follows the increasing intensities of the three bands associated to Cu-OH. Herzog et al. have recently shown using pulse CO_2 electrolysis that the coverage of this *OH layer can be tuned for enhancing ethanol production by changing the anodic and cathodic pulse lengths.[28] Our findings suggest that using CO as the feedstock leads to a significantly higher *OH coverage and a change in CO adsorption configurations compared to what was observed in Herzog's work. A consequent change in the eCORR reactivity can thus be anticipated.

To elucidate the impact of the CO adsorption configuration on the reaction selectivity, product analysis was conducted in a flow cell containing a Cu GDE in 1 M KOH electrolyte (Figure S2). A potential of −1.4 V_{SHE} was selected, as it favors the formation of C_{2+} products.[23] The *FEs* of the major products are presented in Figure 1c (Tables S2-S3). Significant differences are found for acetate and 1-propanol selectivities. Specifically, the *FE* for acetate via eCO_2RR is 1.4%, while it is 10.4% via eCORR. Similarly, the FE of 1-propanol increases from 6.2 to 11.2% when the feedstock was switched from CO_2 to CO.

To better compare the differences in product selectivity formed by eCO_2RR and eCORR, we introduce "*CO-related product selectivity" (CPS) as a performance metric (Supporting Note 1). We define CPS as the ratio of the formation rate of a given product to that of all of the eCO_2RR products, all of which involve *CO as an intermediate. CPS can be used to evaluate products such as ethylene, ethanol, acetate, and 1-propanol.[32] Formate is not included, as it is typically formed via the HCOO* species.[33] Upon switching from CO_2 to CO feedstock, the CPS for acetate increased from 3.4 to 25.1%, and for 1-propanol, from 6.7 to 8.9% (Figure 1d). Conversely, the CPS for other major products such as ethylene and ethanol declined from 59.0 to 44.5% and from 24.7 to 17.4%, respectively, when switching from CO_2 to CO (Figure S6). The difference between eCO_2RR and eCORR has been previously studied.[34−36] These results indicate that compared to eCO_2RR, direct-supplied CO tends to produce more acetate and 1-propanol, which aligns with our current findings. While previous studies generally attribute these differences to variations in pH and CO coverage, our results suggest that the adsorption configuration of CO may also play a role. Specifically, $*CO_B$ appears to favor the production of acetate and 1-propanol, whereas $*CO_L$ seems to favor the formation of ethylene and ethanol.

Comparison of COR Using H-cell and Flow cell. We have previously shown that eCORR on Cu catalysts yielded more acetate in flow cells than in H-cells and have attributed this difference to a higher *CO coverage which favors the reduction of the *CHCO to $CH_2CO_{(g)}$, leading to acetate.[8] Here, we hypothesize that the type of adsorbed *CO formed from eCORR and the presence of coadsorbed *OH might also

https://doi.org/10.1021/jacs.4c08755
J. Am. Chem. Soc. 2024, 146, 30183−30193

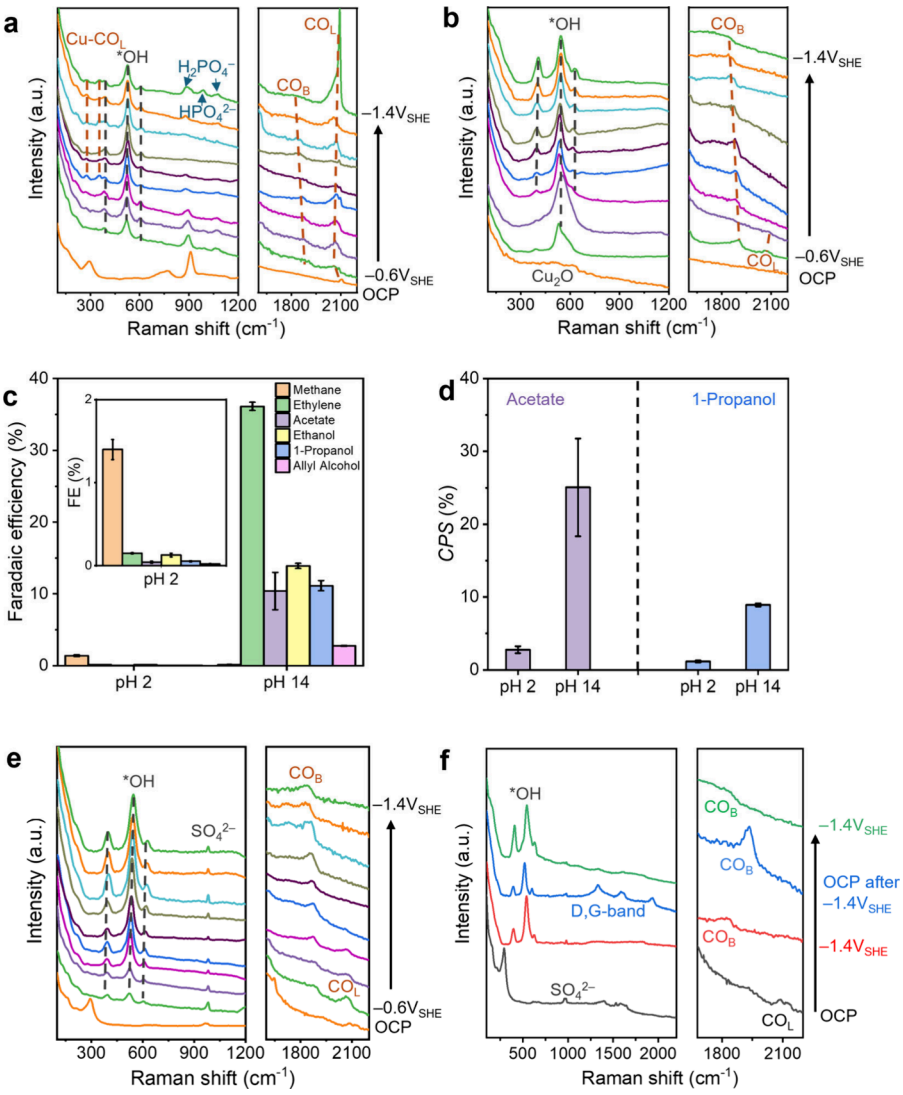

Figure 3. (a,b) Normalized Raman spectra obtained during eCORR on a Cu GDE mounted in a flow cell at OCP and from −0.6 to −1.4 V_{SHE} in (a) 1 M KH_2PO_4 + H_3PO_4 (pH 2) and (b) 1 M KOH (pH 14) electrolytes. Spectra were collected at potential intervals of 0.1 V. (c) Faradaic efficiency of major eCORR products (insert: enlarged part of FE at pH 2) and (d) CPS of acetate and 1-propanol formed on a Cu GDE mounted in a flow cell at −1.4 V_{SHE} in 1 M KH_2PO_4 + H_3PO_4 and 1 M KOH electrolytes. (e) Normalized Raman spectra obtained during eCORR on a Cu GDE mounted in a flow cell at the OCP and from −0.6 to −1.4 V_{SHE} in 0.5 M K_2SO_4 + H_2SO_4 electrolyte (pH 2) (f) Normalized Raman spectra obtained for eCORR on a Cu GDE in a flow cell at −1.4 V_{SHE} in 0.5 M K_2SO_4 + H_2SO_4 electrolyte. CO was continuously flowed into the cell during the experiment. The vibrational frequency of $*CO_B$ shifts due to different *CO coverages and electrode potentials.

influence acetate selectivity. We therefore investigated the surface species formed on Cu GDE in an H-cell and flow cell. 0.5 M K_2SO_4 electrolyte was chosen in lieu of a bicarbonate electrolyte, as we want to completely eliminate the presence of CO_2.

In the H-cell setup, where CO bubbles approach the electrode from the electrolyte, $*CO_L$, characterized by its $\nu_{C\equiv O}$ band at ∼2064 cm^{-1} was observed from −0.6 to −1.1 V_{SHE} (Figure 2a). Shifting the potential to −1.2 V_{SHE} led to the attenuation of the $*CO_L$ signal, indicating a lower $*CO_L$ coverage, likely due to a constrained CO mass transfer within the H-cell. A weak Cu-OH band at ∼532 cm^{-1} was also measured from −1.0 to −1.4 V_{SHE}, suggesting a low *OH coverage. In contrast, when eCORR was performed in a flow cell (where CO flows to the Cu catalyst from the microporous layer side of the carbon paper), a more pronounced Cu-OH band emerged at −0.7 V_{SHE} (Figure 2b). This signal also intensified with a negative shift of the potentials. While the $*CO_L$ signal at 2064 cm^{-1} was observed from −0.6 to −1.0 V_{SHE}, it vanished from −1.1 to −1.4 V_{SHE}, leaving $*CO_B$ at 1842−1865 cm^{-1}.

The *FE*s and CPS of major eCORR products formed at −1.4 V_{SHE} are presented in Figure 2c,d (Tables S4 and S5; Figures S2 and S3). Given the poor CO mass transfer in the H-cell, hydrogen evolution reaction (HER) expectedly dominates with the FE of H_2 exceeding 90%. Switching from H-cell to flow cell increased the CPS for acetate (5.5 to 10.4%) and 1-propanol (5.5 to 8.5%), while the CPS for ethylene and ethanol slightly declined (49.9 to 49.1% and 29.0 to 27.1%, respectively) (Figure S7).

The different current densities exhibited during constant potential electrolysis in the H-cell (∼−14 mA/cm^2) and flow cell (∼−49 mA/cm^2) might cause a difference in the local pH at the Cu surface, therefore changing the product distribution. To rule out the effect of varying currents and local pH on the eCORR product distribution, we conducted constant current

https://doi.org/10.1021/jacs.4c08755
J. Am. Chem. Soc. 2024, 146, 30183−30193

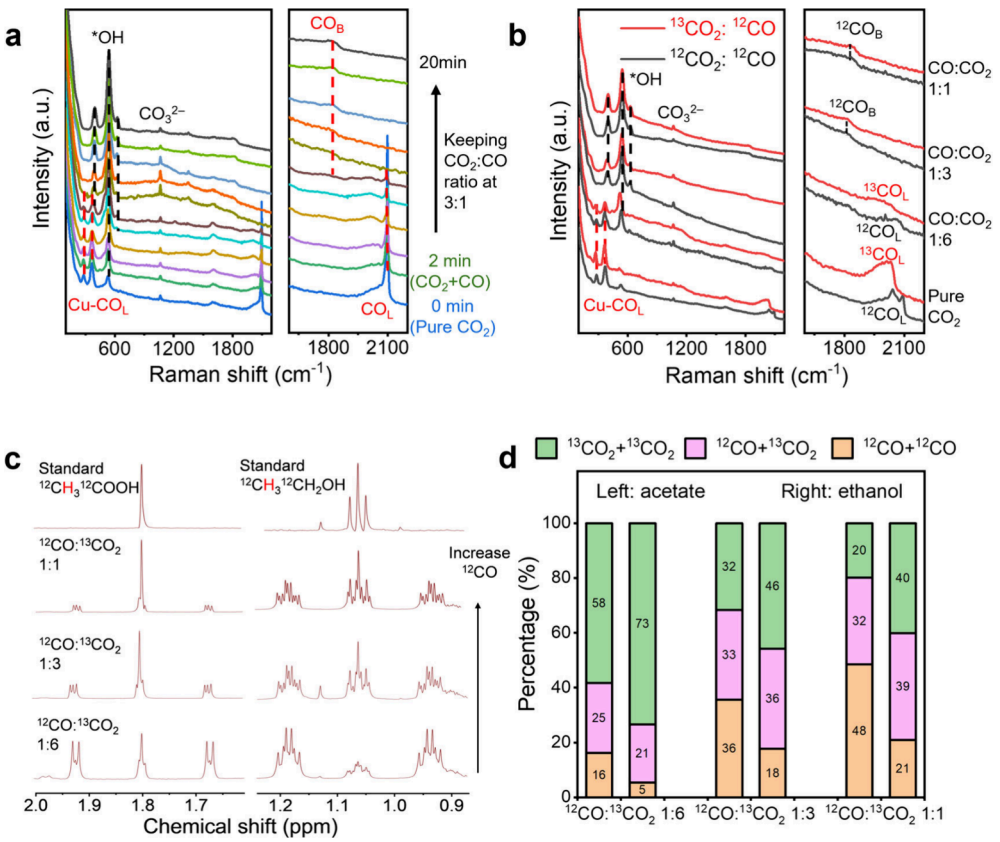

Figure 4. (a) Normalized Raman spectra measured during $CO+CO_2$ (molar ratio 1:3) electrolysis on a Cu GDE mounted in a flow cell in 1 M KOH electrolyte at −1.4 V_{SHE}. Pure CO_2 was first introduced, and a spectrum was collected. After 2 min, a CO_2 and CO mixture (3:1 ratio) was introduced and continuously flowed, and the second spectrum was collected. A spectrum was subsequently acquired every 2 min. (b) Normalized Raman spectra obtained on a Cu GDE mounted in a flow cell in 1 M KOH electrolyte during electrolysis at −1.4 V_{SHE} using $^{12}CO+^{13}CO_2$ at different molar ratios. (c) ^1H NMR spectra of acetate and ethanol formed from $^{12}CO+^{13}CO_2$ electrolysis. (d) Percentage of the amount of acetate and ethanol derived from $^{13}CO_2+^{13}CO_2$, $^{12}CO+^{13}CO_2$, and $^{12}CO+^{12}CO$ during electrolysis of ^{12}CO and $^{13}CO_2$ at 1:6, 1:3, and 1:1 molar ratios (for each electrolysis: left bar, $^{12}CH_3{}^{12}COOH$, orange; $^{13}CH_3{}^{12}COOH$ and $^{12}CH_3{}^{13}COOH$, purple; $^{13}CH_3{}^{13}COOH$, green; right bar, $^{12}CH_3{}^{12}CH_2OH$, orange; $^{13}CH_3{}^{12}CH_2OH$ and $^{12}CH_3{}^{13}CH_2OH$, purple; $^{13}CH_3{}^{13}CH_2OH$, green).

electrolysis in these two types of cells. Both sets of results are consistent with each other: specifically, using constant current electrolysis at −20 mA/cm^2, eCORR in an H-cell still presents lower CPS values of acetate (2.5% to 19.1%) and 1-propanol (2.0% to 11.5%) and higher CPS values of ethylene (52.8% to 47.4%) and ethanol (20.3% to 15.7%), as compared to that in a flow cell (Figure S8). These findings imply a preference to produce acetate and 1-propanol when eCORR was performed within a flow cell configuration with $*CO_B$ adsorbed on the Cu surface. In contrast, $*CO_L$ formed in the H-cell setup favors the generation of ethylene and ethanol.

Comparing COR at Different pH Values. The pH of the electrolyte highly impacts eCORR performances.[25,26] To explore how pH affects CO adsorption configurations on Cu, Raman spectroscopy was conducted on the Cu GDE in 1 M KH_2PO_4 (adjust by H_3PO_4 to pH 2) and in 1 M KOH (pH 14) electrolytes, each within a flow cell (Figure S1).

At pH 2, due to the removal of the oxide layer in the acidic electrolyte, $*CO_L$ can be observed at 2104 cm^{-1} at the OCP. Once the Cu GDE was polarized, bands at 386, 526, and 608 cm^{-1} attributable to Cu-OH species were detected (Figure 3a). Three signals at 884, 988, and 1078 cm^{-1} were also observed. The bands at 884 and 1078 cm^{-1} can be ascribed to $H_2PO_4^-$ ions, while that at 988 cm^{-1} corresponds to HPO_4^{2-} ions (Table S1).[37] When the electrode was polarized from −0.6 V_{SHE} to −1.4 V_{SHE}, two bands at 2065 and 1874 cm^{-1} were observed. These belong respectively to $*CO_L$ and $*CO_B$, with $*CO_L$ being more dominant. In contrast, at pH 14, $*CO_B$ was the only *CO species detected from −0.8 to −1.4 V_{SHE}, with its vibrational frequency shifting with potentials from 1884 to 1826 cm^{-1} (Figure 3b).

Product analysis reveals that at −1.4 V_{SHE}, the formation of eCORR products dominates in KOH electrolyte, while H_2 formation dominates in phosphate electrolyte (Figure 3c and S2; Tables S3 and S6). A notable increase in the CPS of acetate from 2.8% to 25.1% and 1-propanol, from 1.2% to 8.9%, upon changing the electrolyte from phosphate (pH 2) to KOH (pH 14), was found (Figure 3d). Interestingly, despite the adsorption of *CO being mainly in a linear mode in the phosphate electrolyte, the CPS for ethylene and ethanol were 4.9% and 4.1%, respectively, lower than those in KOH (43.5% for ethylene and 16.8% for ethanol). We attribute this reduction in CPS to an increase of H^+ concentration in phosphate electrolyte, which facilitates methane generation.[23] This proposition is supported by a large increase in methane CPS from 0.3% to 59.8% when the electrolyte was switched from alkaline KOH (pH 14) to acidic phosphate (pH 2) (Figure S9).

A change in CO adsorption was also observed when we switched from phosphate to sulfate electrolyte while

https://doi.org/10.1021/jacs.4c08755
J. Am. Chem. Soc. 2024, 146, 30183−30193

maintaining the same bulk pH of 2. In the sulfate electrolyte, a $*CO_L$ signal at 2045−2150 cm^{-1} was detected at OCP (Figure 3e). As the electrode potential became more negative, $*CO_B$ predominantly adsorbed onto the Cu surface. We conjectured that this shift in CO adsorption configuration may be due to the local pH turning more alkaline in sulfate electrolyte during the eCORR.[18] This is because H_2SO_4/K_2SO_4 electrolyte is not as good a buffer as H_3PO_4/KH_2PO_4.[38,39] Product analysis further reveals an increase in the FEs of eCORR products formed in the sulfate electrolyte, as compared to in the phosphate electrolyte (Table S7 and Figure S10). There is also an enhancement in CPS for acetate and 1-propanol, which at 13.4 and 8.9% respectively in the sulfate environment, marks a significant increase from the 2.8 and 1.2% observed in the phosphate electrolyte (Figure 3d and Figure S11).

It is noteworthy that during our Raman experiment in sulfate electrolyte, the Cu-OH formed during the electrolysis persisted even after the electrolysis had ended (blue spectrum, Figure 3f). Intriguingly, $*CO_B$ at 1930 cm^{-1} could also be detected, evidence of an alteration in the stable *CO adsorption configuration by *OH species on the Cu surface. Collectively, these observations indicate that the presence of Cu-OH species shifts the binding of *CO from linear to bridged (Figure 3e,f). Upon reapplication of the potential at −1.4 V_{SHE}, a pronounced decrease in the intensity of $*CO_B$ was observed, indicating its electroreduction (green-colored spectrum, Figure 3f). These findings not only highlight the importance of Cu surface characteristics in determining CO adsorption configurations but also affirm the involvement of $*CO_B$ as active eCORR intermediates.

Electrochemical Reduction of CO+CO_2 Feeds. The electrochemical reduction of a CO+CO_2 feed has been found effective for boosting the production rate of C_{2+} products.[40−43] Gao et al. suggested that eCORR and eCO_2RR could have taken place on different Cu sites.[42] To understand the CO adsorption configuration in a flow cell during the electrolysis of a CO+CO_2 feed, Raman spectroscopy was performed on a Cu GDE mounted in a flow cell with a 1 M KOH electrolyte. The Raman spectrum of the electrode biased at −1.4 V_{SHE} was first recorded, with pure CO_2 being supplied from the gas chamber. A mixture of CO+CO_2 gas at a molar ratio of 1:3 then replaced the CO_2 feed. When pure CO_2 was supplied, the generated CO intermediate adsorbed on the Cu surface linearly, as indicated by its $\nu_{C\equiv O}$ signal at 2093 cm^{-1} (Figure 4a). A weak band at 530 cm^{-1} that can be attributed to Cu-OH was also observed. When the gas feed was switched to a CO_2+CO mixture, the intensity of the Cu-OH band at 530−538 cm^{-1} increased. Two additional bands of Cu-OH at 393 and 623 cm^{-1} also became discernible over time. Concurrently, the 2093 cm^{-1} band of $*CO_L$ attenuates, while a $*CO_B$ band at 1821 cm^{-1} emerges. The attenuation of the $*CO_L$ signal might result from the evolution of Cu-OH.

To determine the proportion of $*CO_B$ originating from directly supplied CO versus CO produced from CO_2, $^{13}CO_2$ and ^{12}CO was utilized. A constant potential of −1.4 V_{SHE} was applied. When pure $^{13}CO_2$ was used, the $*^{13}CO_L$ generated from $^{13}CO_2$ displayed a distinct band at 2030 cm^{-1}, red-shifted from 2093 cm^{-1} of $*^{12}CO_L$ due to mass difference between the isotopes (Figure 4b). Upon introduction of ^{12}CO into the $^{13}CO_2$ at a molar ratio of 1:6, a decline in the intensity of the $*^{13}CO_L$ band was observed, in comparison to the pure e$^{13}CO_2$RR experiment. A further increase in the concentration of ^{12}CO resulted in the complete disappearance of $*^{13}CO_L$ signals. $*^{12}CO_B$ was detected instead, as signified by its signal at 1821 cm^{-1}. Strikingly, the $*^{12}CO_B$ band maintained the same vibration frequency at 1821 cm^{-1}, even with a ^{12}CO:$^{13}CO_2$ molar ratio of 1:3, indicating that all $*CO_B$ was derived exclusively from ^{12}CO.

The spectra measured during the co-electrolysis of N_2 and CO at −1.4 V_{SHE} were also compared (Figures S12 and S13). When pure N_2 was utilized, a Cu-OH band was present at 533 cm^{-1}, suggesting that Cu-OH was formed during HER. The introduction of a small proportion of CO, at a CO:N_2 molar ratio of 1:6 resulted in a significant enhancement of the Cu-OH band, as compared to that in pure N_2. Spectra measured at a constant applied current of −50 mA/cm^2 in CO- and N_2-saturated 1 M KOH electrolyte (thereby keeping the local pH similar) also showed that directly supplied CO better facilitates the formation of Cu-OH (Figure S14). Meanwhile, $*CO_B$ was adsorbed on the Cu surface during the co-electrolysis of CO and N_2 at ratios from 1:6 to 1:1, as evident by its signal at 1821 cm^{-1} (Figure S12). This observation further indicates that the $*CO_L$ measured during CO+CO_2 electrolysis originates from CO_2, while $*CO_B$ is derived from directly supplied CO.

To elucidate how different CO adsorption configurations and formation of Cu-OH impact product selectivity, we electrolyzed a ^{12}CO+$^{13}CO_2$ mixture on a Cu GDE at −1.4 V_{SHE} in a flow cell and analyzed the liquid products using ^1H NMR spectroscopy. The presence of ^{13}C in the products resulted in NMR spectral splitting distinct from that of standard ^{12}C acetate and ethanol (Figure 4c and Figure S15). This isotopic splitting allows us to quantify acetate and ethanol derived from $^{13}CO_2$ and ^{12}CO (Figure 4d and Table S8). We found a smaller presence of ^{13}C in acetate compared to ethanol, suggesting that acetate primarily originates from directly supplied ^{12}CO, whereas ethanol is largely derived from ^{13}CO produced via e$^{13}CO_2$RR. Taking the electrolysis of a ^{12}CO:$^{13}CO_2$ mixture with a molar ratio of 1:1 as an example, the coupling of directly fed ^{12}CO contributes to 48% of the total acetate yield. In contrast, only 20% of acetate originates from the coupling of ^{13}CO-^{13}CO produced from $^{13}CO_2$. Conversely, only 21% of ethanol comes from the coupling of directly fed ^{12}CO, whereas a substantial 40% of ethanol is generated from ^{13}CO formed from $^{13}CO_2$.

The composition of 1-propanol with different amounts of ^{13}C makes peak assignment and quantification challenging. Consequently, we could only give an estimate by integrating the broad peaks of ^{13}C and ^{12}C of 1-propanol (Figure S16, Table S9). The findings reveal that, similar to acetate, the proportion of ^{13}C in 1-propanol is smaller (52.8%) compared to that of ethanol (60.8%) when cofeeding ^{12}CO:$^{13}CO_2$ with a molar ratio of 1:1. This suggests that compared to $*CO_L$, $*CO_B$ converts more easily to 1-propanol.

Modeling the Cu Surface with Coadsorbed *OH and *CO. To assign the Raman bands, we simulate the linear, bridge, and hollow adsorption of *OH on the Cu(100) and Cu(111) facets (Supporting Note 2). The experimentally detected band at 525−545 cm^{-1} can be assigned to the Cu-OH bending mode (ν_1) of both bridged $*OH_B$ on Cu(100) and hollow $*OH_H$ on Cu(111) (Figure S17), with the former species being slightly more stable (Table S10). The band at 608−640 cm^{-1} also corresponds to the ν_1 mode for $*OH_H$, albeit it is adsorbed on Cu(100). The band at 386−406 cm^{-1} can be assigned to the Cu-OH stretching mode (ν_2) of $*OH_B$

https://doi.org/10.1021/jacs.4c08755
J. Am. Chem. Soc. 2024, 146, 30183−30193

on either Cu(100) or Cu(111). Overall, we consider $*OH_B$ on Cu(100) to be the dominant species.

To further understand how *OH at a higher coverage arranges on surfaces, we computed the differential Gibbs free energies ($d\Delta G_{*OH}$) of a second $*OH_B$, and we found that their coadsorption is highly stabilized due to hydrogen bonding (Figure S18). Differential adsorption energies of subsequent *OH species (third and fourth) show that at even higher coverages, *OH is adsorbed on Cu(100) with enhanced stability in linear stripes; however, no significant stabilization effect could be observed for *OH on Cu(111) (Figures S18b and S19). Considering the lateral repulsion between two *OH at adjacent bridge sites sharing one single Cu atom (Structure 1 in Figure S18c, $\Delta\Delta G_{ads}$ differential = 0.53 eV with respect to the adsorption energy of a single $*OH_B$), the bridge sites near the *OH stripes are likely to be unoccupied. Therefore, we build two periodic models with one and two empty spaces between stripes (θ_{OH} = 1/2 and 1/3 ML, respectively) (Figure 5a). To assess how the presence of these *OH stripes affects

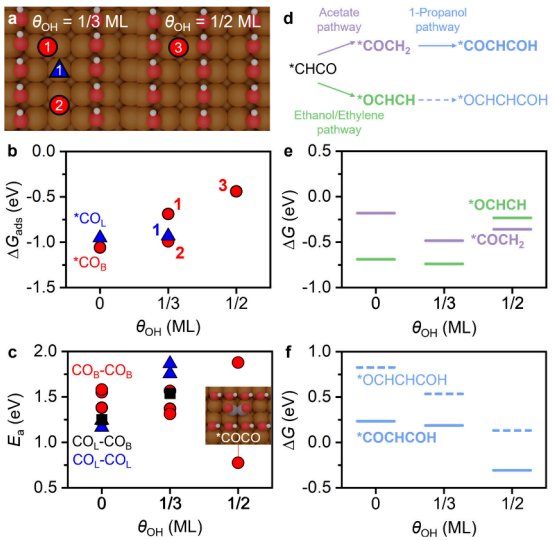

Figure 5. (a) Cu(100) models with adsorbed $*OH_B$ stripes at medium (θ_{OH} = 1/3 ML) and high coverages (θ_{OH} = 1/2 ML). Red circles and blue triangles indicate the active sites for (b) Gibbs free energies of $*CO_B$ and $*CO_L$ adsorption for different OH coverages (θ_{OH} = 0, 1/3, and 1/2 ML) at $U = -1.4$ V_{SHE}. (c) CO-CO coupling energy barriers for CO_L-CO_L, CO_L-CO_B, and CO_B-CO_B (in blue, black, and red, respectively) for the different θ_{OH} values studied. The inset panel represents the *COCO final state configuration of the most favored CO_B-CO_B coupling at θ_{OH} = 1/2 ML. (d) Scheme of key intermediates leading to acetate, ethylene, ethanol, and 1-propanol. Gibbs free energies for the rate determining steps for (e) $*COCH_2$ (leading to acetate) vs *OCHCH (leading to ethylene/ethanol) production and (f) 1-propanol production at $U = -1.4$ V_{SHE}. Continuous and dashed lines represent 2 different C_3 intermediates (from $*COCH_2$ and *OCHCH, respectively) leading to 1-propanol. For (a) and (c), Cu, O, H, and C atoms are depicted by brown, red, white, and gray spheres, respectively.

*CO adsorption, we computed the adsorption energies of $*CO_L$ and $*CO_B$ species on models with zero, medium, and high *OH coverages (θ_{OH} = 0, 1/3, and 1/2 ML; Figure 5b). As *OH hinders *CO adsorption at distances smaller than 3.0 Å (Figure S20a), in the narrow space between stripes at θ_{OH} = 1/2 ML, $*CO_L$ adsorption sites are blocked and only $*CO_B$ adsorption is feasible (ΔG_{ads} = −0.44 eV). Therefore, $*CO_L$ domains are broken at high *OH coverages, thus confining CO adsorption to only bridge sites, in line with the $*CO_L$ shift to $*CO_B$ observed in our experiments (Figure 3f). Note that this shift is not expected for *CO originating from the eCO_2RR, as adsorbed CO_2 inhibits *OH adsorption on its vicinities, thus limiting the formation of *OH stripes (Figure S21).

To further clarify how *CO enhances *OH adsorption, we conducted DFT simulations at different $*CO_L$ and $*CO_B$ coverages (0−0.5 ML) on Cu(100). Bader charge analysis indicates a positive polarization of these surfaces as the amount of *CO increases (Figure S22), which suggests *CO will promote the adsorption of an anion such as OH^- due to ionic interactions.[44] While a previous work has suggested that the effect of CO in promoting Cu-OH formation is due primarily to the decomposition of surface water facilitated by eCORR, our results indicate that surface polarization also plays an important role in Cu-OH formation.[21]

We computed the coadsorption energies of $*CO_L$ + $*CO_L$, $*CO_B$ + $*CO_B$, and $*CO_L$ + $*CO_B$, which showed no repulsion at distances greater than 3.0 Å. This indicates that on these confined domains $*CO_L$ or $*CO_B$ can stably coadsorb close enough to each other to facilitate further CO-CO coupling (Figure S20b). The computed and scaled $\nu_{C\equiv O}$ frequencies for $*CO_L$ and $*CO_B$ on Cu(100) also agree with detected Raman bands (2027 and 1884 cm^{-1} for $*CO_L$ and $*CO_B$, respectively; Table S11).

DFT Simulation of CO-CO Coupling to C_{2+} Products. We computed the CO-CO coupling energy barriers for $*CO_B$ and $*CO_L$ domains in θ_{OH} = 0, 1/3, and 1/2 ML, using the climbing image nudged elastic band (CI-NEB) method (Figures 5c and Figures S23−S25). For a Cu(100) surface without *OH, the lowest energy barriers were observed for coupling reactions involving one or two $*CO_L$ (CO_L-CO_L and CO_L-CO_B), in line with previous results.[29] At θ_{OH} = 1/3 ML, the CO_B-CO_B coupling became favored. For the confined $*CO_B$ domains at θ_{OH} = 1/2 ML, we found the lowest CO-CO coupling energy barrier of E_a = 0.77 eV and a more stable final state configuration of *COCO than *OCCO (Figures S24 and S25). In contrast, the *OCCO intermediate was more stable than *COCO on surfaces with lower *OH coverage (θ_{OH} = 0 and 1/3 ML). We note that these findings can explain the observed decrease in FE of ethanol and ethylene when using CO as a feedstock compared to CO_2 (Figure 1c), as $*CO_B$ on confined domains will not evolve easily to the *OCCO intermediate which leads to ethylene and ethanol.[32]

To further elucidate how changes in *CO adsorption configurations affect the reactivity, we computed the adsorption energies of key intermediates leading to acetate, ethylene/ethanol, and 1-propanol on Cu(100) surfaces with the three *OH coverages θ_{OH} = 0, 1/3, and 1/2 ML (Figure 5d). From the common intermediate *CHCO, the energies of a further hydrogenation step to $*COCH_2$ or *OCHCH serve as indicators of acetate and ethylene/ethanol selectivity, respectively.[32] The *OCHCH intermediate is favored over $*COCH_2$ for θ_{OH} = 0 and 1/3 ML. However, *OCHCH becomes less stable at θ_{OH} = 1/2 ML, compared to θ_{OH} = 0 and 1/3 ML ($\Delta\Delta G$ = 0.46 and 0.51 eV). $*COCH_2$, instead, becomes the dominant species, thus shifting selectivity toward acetate (Figure 5e). The energy profiles for these competing reaction pathways for acetate and ethanol indicate that both are thermodynamically downhill at $U = -1.4$ V_{SHE}, with acetate becoming more favored at θ_{OH} = 1/2 ML (Figure S26).

https://doi.org/10.1021/jacs.4c08755
J. Am. Chem. Soc. 2024, 146, 30183−30193

Interestingly, both *$COCH_2$ (acetate pathway) and *OCHCH (ethanol pathway) intermediates can further couple with a neighboring *CO (generating *COCHCOH and *OCHCHCOH, respectively), leading to 1-propanol. For all three studied θ_{OH} coverages, we found that *COCHCOH is more stable than *OCHCHCOH, which indicates that the acetate pathway is more likely to contribute to 1-propanol formation. While both *COCHCOH and *OCHCHCOH are not thermodynamically favored at θ_{OH} of 0 and 1/3 ML, the coupling reaction to *COCHCOH becomes exergonic (ΔG = −0.31 eV) at θ_{OH} = 1/2 ML (Figure 5f). Collectively, this means that as the *OH coverage increases to 1/2 ML, active *CO_B domains are generated, favoring both acetate and 1-propanol production (Scheme 1), which aligns well with our experimental observations of reactivity (Figures 1d, 2d, and 3d).

Scheme 1. Correlation between Increase of OH Coverage (θ_{OH}), *CO Adsorption Configuration Shifting from *CO_L to *CO_B, and Changes in Selectivity from Ethylene and Ethanol Production to Acetate and 1-Propanol[a]**

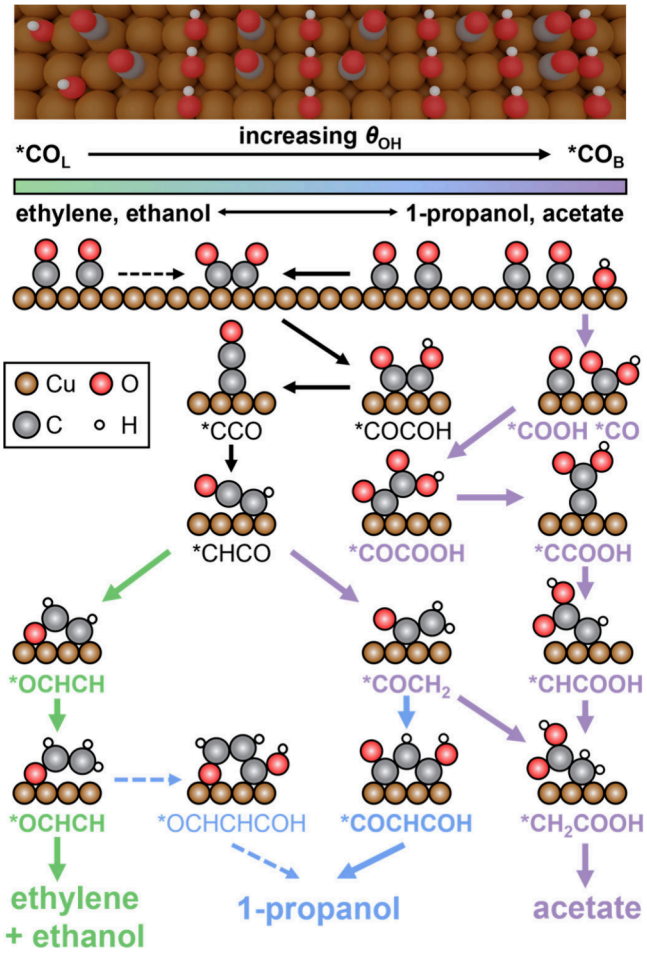

[a]Unfavored pathways are indicated by dotted lines.

We also consider a newly reported mechanism for acetate production, which states that *CO first couples with *OH to form *COOH, which then further couples with a second *CO to give *COCOOH.[45] The first coupling with *OH_B showed lower barriers for *CO_B (E_a = 0.52 eV for θ_{OH} = 0 ML, and E_a = 0.61 eV for θ_{OH} = 1/2 ML) than for *CO_L (E_a = 0.72−0.82 eV); the second CO-COOH coupling was more favored in θ_{OH} = 1/2 ML (E_a = 0.83 eV) confined domains compared to that in θ_{OH} = 0 ML (E_a = 1.18 eV). The complete reaction pathway is energetically favorable for both θ_{OH} = 0 and 1/2 ML (Figure S27), indicating that acetate can alternatively be formed from this path.

CONCLUSION

We have revealed the critical role of *CO_B as an active intermediate in the eCO_2RR on Cu catalysts. Combining *in situ* Raman spectroscopy and product analysis, supported by isotope-labeled $^{12}CO+^{13}CO_2$ co-electrolysis experiments, we demonstrate that *CO_B distinctly reacts to give acetate and 1-propanol, while *CO_L favors ethylene and ethanol formation. DFT simulations further unveiled that *CO promotes the formation of Cu-OH, and high *OH coverages confine CO adsorption to a bridge configuration. Within these confined domains, the activation energy for CO_B-CO_B coupling significantly decreases, as compared to on surfaces without *OH. This confinement further facilitates the formation of *$COCH_2$ from the CO-CO dimer and stabilizes the *COCHCOH intermediate, thus respectively favoring the production of acetate and 1-propanol. These insights not only advance our understanding of the mechanistic pathways occurring during eCO_2RR but also highlight the potential of optimizing reaction conditions or catalysts to steer the formation of specific multicarbon products.

EXPERIMENTAL SECTION

Electrochemical Deposited Cu GDE Preparation and Characterization. An ∼200 nm thick Cu (99.99%, Latech Scientific Supply) film was sputtered (Denton Instrument; sputtering radio frequency power of 100 W for 1000 s) onto a carbon gas diffusion layer substrate (GDL, Sigracet 28 BC). To ensure good reproducibility of the results and improve the strength of the Raman signal, another Cu layer was then electrochemically deposited on the GDL at a constant current density of −200 mA/cm^2 for 20 s in 0.4 M $CuSO_4$ (98.5%, GCE) + 0.2 M H_2SO_4 (95%, VWR) solution. After Cu deposition, the electrode surface was protected by a thin layer of ultrapure water (18.2 MΩ, Sartorius) and quickly transferred to the cell for electrochemical measurements and Raman spectroscopy. The morphologies of the Cu GDE samples were characterized by scanning electron microscopy (SEM, JEOL JSM 6710 F; 1.91 × 10^{-5} Pa; accelerating voltage of 5.0 kV; probe current of 8 pA; working distance of 7.9 mm) (Figure S28).

Electrochemical Measurements. Electrochemical measurements were conducted using either a flow-cell or a H-cell setup (Figures S2 and S3). The cathodic and anodic compartments of the cell were separated by an anion exchange membrane (Selemion AMV, AGC, Asahi Glass) when the electrolyte was alkaline and neutral or a cation exchange membrane (Nafion 117, DuPont) when the electrolyte was acidic. Ag/AgCl (saturated KCl, Pine) was employed as the reference electrode. When testing in alkaline electrolyte, Ni foam (99.0%, 120 ppi, 1.0 mm thickness, Xiamen Lith Machine Limited) was used as the counter electrode. When testing in acidic and neutral electrolytes, an IrO_2/Ti foam counter electrode was used.

A potentiostat (Gamry reference 600) was used to control and measure the electrochemical activity. The current interrupt mode was used to compensate for the *iR* drop during constant potential electrolysis. CO/CO_2 electrolysis was conducted in 1 M KOH (pH = 14, 99.999%, Meryer Chemical Technology), 0.5 M K_2SO_4 (pH = 7, 99.999%, Meryer Chemical Technology), or 1 M KH_2PO_4+H_3PO_4 (pH = 2, 99.999%, Meryer Chemical Technology) electrolyte. CO (99.97%, Linde)/CO_2 (99.999%, Linde) was introduced to the flow cell at a flow rate of 10 mL min^{-1} using a mass flow controller (Alicat Scientific). The flow rates of the inlet and outlet gases were monitored

https://doi.org/10.1021/jacs.4c08755
J. Am. Chem. Soc. 2024, 146, 30183−30193

to avoid any gas leak. The electrolysis period was 43 min to ensure at least 4 injections of gas products into the GC. All potentials in this work are referenced to the standard hydrogen electrode (SHE) using the average potential of the Ag/AgCl electrode ($E_{Ag/AgCl}$)

$$E_{SHE} = E_{Ag/AgCl} + 0.197$$

For eCORR H-cell testing, a homemade H-cell (3 mL catholyte) was used for the electrochemical measurements and product analysis (Figures S3 and S29). An anion membrane (Selemion AMV, AGC Asahi Glass) was used to separate the anolyte and catholyte. CO was bubbled into the H-cell at a flow rate of 5 mL min^{-1} (Alicat Scientific).

For the ^{13}C experiment, the same protocol as that used for the ^{12}C experiment was applied. The ratio of $^{13}CO_2$ (^{13}C, 99%, Cambridge Isotope Lab) and ^{12}CO (99.97%, Linde) was controlled by a mass flow controller (Alicat Scientific).

Product Analysis. Gaseous products formed during eCORR and eCO_2RR were analyzed using an online gas chromatograph (Shimadzu GC2014) equipped with one thermal conductivity detector (TCD) and two flame ionization detectors (FIDs). One of the FIDs has a methanizer. Four GC injections of gas samples (intervals of 810 s between consecutive injections) were made. To ensure that the reported data are from a system under equilibrium, only measurements from the second to fourth injections were used for analyses. The product concentrations were stable between these injections. Each set of data was collected from measurements made on at least three independently prepared samples. The liquid products were analyzed by a headspace gas chromatograph (Headspace GC, Agilent 7697A) with a FID (detection limit <0.2 μM). Acetate and formate were quantified using high-performance liquid chromatography (HPLC, Agilent-1260 Infinity Series; Aminex HPX-87H column; variable wavelength detector; and 0.5 mM H_2SO_4 mobile phase).

GC chromatograms of standards and a representative eCO_2RR sample are shown in Figure S30. The liquid-phase product analyses from a Raman electrochemical cell (Figure S1) and a typical flow cell (Figure S2) were also compared. While small differences in Faradaic efficiencies of the products were observed (Figure S31a), the overall product distribution in the liquid phase remained consistent (Figure S31b). This suggests that the results from the Raman cell are representative of those in a typical flow cell.

For ^{13}C measurements, ^1H NMR (Bruker Avance DRX500(2D)) were used to quantify the product ratio of ^{13}C and ^{12}C in CH_3COOH and CH_3CH_2OH. Typically, 520 μL of the catholyte was mixed with 20 μL of an internal standard consisting of 25 mM phenol (99.6%, VWR) and 5 mM dimethyl sulfoxide (99.9%, Quality Reagent Chemical). 60 μL of D_2O (99.9% deuterium, Merck Millipore) was then added into 0.5 mL of this mixture. Solvent suppression protocol was used to decrease the intensity of the water peak. 516 continuous scans were used to improve the signal-to-noise ratio.

***In Situ* Raman Experiment.** A LabRAM HR Evolution Raman microscope (Horiba) equipped with a He-Ne laser (λ = 633 nm) was employed. A homemade Raman electrochemical cell was used (Figure S1). A Ag/AgCl (saturated KCl, Pine) was used as the reference electrode, and a Ni foam (for alkaline electrolyte) or Pt wire (for an acidic electrolyte) was used as the counter electrode. In the flow cell test, the gas was introduced into the gas chamber at a flow rate of 10 mL min^{-1}. During the H-cell type test, the electrolyte was presaturated with CO for 30 min and CO was bubbled into the electrolyte throughout the experiment. A water immersion objective (LOMO, 40×, numerical aperture = 1.23) was used to focus and collect the incident and scattered laser.[22] A 0.013 mm thick optically transparent Teflon film (American Durafilm) was tightly wrapped over the objective to protect it from any corrosive electrolyte. Each spectrum was acquired over 8 s. Ten spectra were collected and averaged to improve the signal-to-noise ratio of the presented spectrum.

COMPUTATIONAL DETAILS

Density functional theory (DFT) simulations were carried out with Vienna Ab Initio Simulation Package (VASP 5.4.4) to obtain adsorption energies of key intermediates.[46,47] The exchange functional used was the Perdew–Burke–Emzerhof (PBE).[48] Dispersion was included though the DFT-D2 method[49,50] with our reparametrized C_6 coefficients for Cu atoms.[51] Inner electrons were represented by projector augment wave (PAW),[52,53] while the valence monoelectronic states were expanded as plane waves with a kinetic energy cutoff of 450 eV. For all the investigated systems, structures were relaxed using convergence criteria of 0.03 eV/Å and 10^{-5} eV for the ionic and electronic steps, respectively. The vacuum thickness between periodic repetitions on the z direction accounted for at least 10 Å. We sampled the Brillouin zone by a Γ-centered k-point mesh from the Monkhorst–Pack method[54] with a reciprocal grid size smaller than $0.03 \cdot 2\pi$ $Å^{-1}$. The slab models were asymmetric, and thus the dipole correction was applied.[55] Reported adsorption energies were obtained using CO_2(g), H_2(g), H_2O(g), and clean surfaces as energy references. The computational hydrogen electrode (CHE) was used for obtaining the relative energy between H^+ and gas-phase H_2 at U = 0.0 V and pH = 0.[56,57] To find transition states for different CO-CO coupling reactions, the climbing image nudged elastic band (CI-NEB) method was employed.[58] Their transition state nature was confirmed by computing numerical frequencies with a step size of ± 0.015 Å.

ASSOCIATED CONTENT

Data Availability Statement

Supporting DFT data sets are available in ioChem-BD[59] at https://doi.org/10.19061/iochem-bd-1-315. All other raw data are available from the corresponding author upon reasonable request.

Supporting Information

The Supporting Information is available free of charge at https://pubs.acs.org/doi/10.1021/jacs.4c08755.

Supplementary figures, SEM images of samples before and after reactions, GC and HPLC data, electrochemical data, NMR spectra and analysis, notes on the calculation of CPS, and DFT simulations details (PDF)

AUTHOR INFORMATION

Corresponding Authors

Núria López − *Institute of Chemical Research of Catalonia (ICIQ-CERCA), The Barcelona Institute of Science and Technology (BIST), 43007 Tarragona, Spain;* orcid.org/0000-0001-9150-5941; Email: nlopez@iciq.es

Boon Siang Yeo − *Department of Chemistry, Faculty of Science, National University of Singapore, Singapore 117543, Singapore;* orcid.org/0000-0003-1609-0867; Email: chmyeos@nus.edu.sg

Authors

Haibin Ma − *Department of Chemistry, Faculty of Science, National University of Singapore, Singapore 117543, Singapore*

Enric Ibáñez-Alé − *Institute of Chemical Research of Catalonia (ICIQ-CERCA), The Barcelona Institute of Science and Technology (BIST), 43007 Tarragona, Spain; Universitat Rovira i Virgili, 43002 Tarragona, Spain*

Futian You − *Department of Chemistry, Faculty of Science, National University of Singapore, Singapore 117543, Singapore*

Complete contact information is available at: https://pubs.acs.org/10.1021/jacs.4c08755

Author Contributions

H.M. and E.I.-A. contributed equally.

Notes

The authors declare no competing financial interest.

■ ACKNOWLEDGMENTS

The authors thank the National Research Foundation of Singapore (Urban Solutions and Sustainability, Industry Alignment Fund (Pre-Positioning) Programme, A-0004543-00-00) and the Spanish Ministry of Science and Innovation (PRE2021-097615, PID2021-122516OB-I00, Severo Ochoa Centre of Excellence CEX2019-000925-S 10.13039/501100011033) for the financial support of this project. The Barcelona Supercomputing Centre-Mare Nostrum (BSC-RES) is acknowledged for providing generous computational resources.

■ REFERENCES

(1) Bushuyev, O. S.; De Luna, P.; Dinh, C. T.; Tao, L.; Saur, G.; van de Lagemaat, J.; Kelley, S. O.; Sargent, E. H. What should we make with CO_2 and how can we make it? *Joule* **2018**, *2* (5), 825−832.

(2) Kortlever, R.; Shen, J.; Schouten, K. J. P.; Calle-Vallejo, F.; Koper, M. T. Catalysts and reaction pathways for the electrochemical reduction of carbon dioxide. *J. Phys. Chem. Lett.* **2015**, *6* (20), 4073−4082.

(3) Jiang, S.; Klingan, K.; Pasquini, C.; Dau, H. New aspects of operando Raman spectroscopy applied to electrochemical CO_2 reduction on Cu foams. *J. Chem. Phys.* **2019**, *150* (4), 041718.

(4) Lee, S. Y.; Kim, J.; Bak, G.; Lee, E.; Kim, D.; Yoo, S.; Kim, J.; Yun, H.; Hwang, Y. J. Probing Cation Effects on *CO Intermediates from Electroreduction of CO_2 through Operando Raman Spectroscopy. *J. Am. Chem. Soc.* **2023**, *145* (42), 23068−23075.

(5) Gunathunge, C. M.; Li, J.; Li, X.; Hong, J. J.; Waegele, M. M. Revealing the predominant surface facets of rough Cu electrodes under electrochemical conditions. *ACS Catal.* **2020**, *10* (12), 6908−6923.

(6) An, H.; Wu, L.; Mandemaker, L. D.; Yang, S.; de Ruiter, J.; Wijten, J. H.; Janssens, J. C.; Hartman, T.; van der Stam, W.; Weckhuysen, B. M. Sub-second time-resolved surface-enhanced Raman spectroscopy reveals dynamic CO intermediates during electrochemical CO_2 reduction on copper. *Angew. Chem., Int. Ed.* **2021**, *60* (30), 16576−16584.

(7) Sandberg, R. B.; Montoya, J. H.; Chan, K.; Nørskov, J. K. CO-CO coupling on Cu facets: Coverage, strain and field effects. *Surf. Sci.* **2016**, *654*, 56−62.

(8) You, F.; Urrego-Ortiz, R.; Pan, S. S. W.; Calle-Vallejo, F.; Yeo, B. S. Adsorbate Coverage Effects on the Electroreduction of CO to Acetate. *Appl. Catal. B: Environ.* **2024**, *352*, 124008.

(9) Goodpaster, J. D.; Bell, A. T.; Head-Gordon, M. Identification of possible pathways for C−C bond formation during electrochemical reduction of CO_2: new theoretical insights from an improved electrochemical model. *J. Phys. Chem. Lett.* **2016**, *7* (8), 1471−1477.

(10) Yang, L.; Lv, X.; Peng, C.; Kong, S.; Huang, F.; Tang, Y.; Zhang, L.; Zheng, G. Promoting CO_2 Electroreduction to Acetate by an Amine-Terminal, Dendrimer-Functionalized Cu Catalyst. *ACS Cent. Sci.* **2023**, *9* (10), 1905−1912.

(11) Cai, Y.; Yang, R.; Fu, J.; Li, Z.; Xie, L.; Li, K.; Chang, Y.-C.; Ding, S.; Lyu, Z.; Zhang, J.-R.; et al. Self-pressurizing nanoscale capsule catalysts for CO_2 electroreduction to acetate or propanol. *Nat. Synth.* **2024**, *3*, 891−902.

(12) Shao, F.; Wong, J. K.; Low, Q. H.; Iannuzzi, M.; Li, J.; Lan, J. In situ spectroelectrochemical probing of CO redox landscape on copper single-crystal surfaces. *Proc. Natl. Acad. Sci. U.S.A.* **2022**, *119* (29), e2118166119.

(13) Salimon, J.; Hernández-Romero, R.; Kalaji, M. The dynamics of the conversion of linear to bridge bonded CO on Cu. *J. Electroanal. Chem.* **2002**, *538*, 99−108.

(14) Liu, Q.; Jiang, Q.; Li, L.; Yang, W. Spontaneous Reconstruction of Copper Active Sites during the Alkaline CORR: Degradation and Recovery of the Performance. *J. Am. Chem. Soc.* **2024**, *146* (6), 4242−4251.

(15) Gunathunge, C. M.; Ovalle, V. J.; Li, Y.; Janik, M. J.; Waegele, M. M. Existence of an electrochemically inert CO population on Cu electrodes in alkaline pH. *ACS Catal.* **2018**, *8* (8), 7507−7516.

(16) Chang, X.; Vijay, S.; Zhao, Y.; Oliveira, N. J.; Chan, K.; Xu, B. Understanding the complementarities of surface-enhanced infrared and Raman spectroscopies in CO adsorption and electrochemical reduction. *Nat. Commun.* **2022**, *13* (1), 2656.

(17) Zhao, Y.; Chang, X.; Malkani, A. S.; Yang, X.; Thompson, L.; Jiao, F.; Xu, B. Speciation of Cu surfaces during the electrochemical CO reduction reaction. *J. Am. Chem. Soc.* **2020**, *142* (21), 9735−9743.

(18) Chang, X.; Zhao, Y.; Xu, B. pH dependence of Cu surface speciation in the electrochemical CO reduction reaction. *ACS Catal.* **2020**, *10* (23), 13737−13747.

(19) Kibria, M. G.; Edwards, J. P.; Gabardo, C. M.; Dinh, C. T.; Seifitokaldani, A.; Sinton, D.; Sargent, E. H. Electrochemical CO_2 reduction into chemical feedstocks: from mechanistic electrocatalysis models to system design. *Adv. Mater.* **2019**, *31* (31), 1807166.

(20) Burdyny, T.; Smith, W. A. CO_2 reduction on gas-diffusion electrodes and why catalytic performance must be assessed at commercially-relevant conditions. *Environ. Sci. Technol.* **2019**, *12* (5), 1442−1453.

(21) Shao, F.; Xia, Z.; You, F.; Wong, J. K.; Low, Q. H.; Xiao, H.; Yeo, B. S. Surface Water as an Initial Proton Source for the Electrochemical CO Reduction Reaction on Copper Surfaces. *Angew. Chem., Int. Ed.* **2023**, *62* (3), e202214210.

(22) Deng, Y.; Handoko, A. D.; Du, Y.; Xi, S.; Yeo, B. S. In situ Raman spectroscopy of copper and copper oxide surfaces during electrochemical oxygen evolution reaction: identification of Cu(III) oxides as catalytically active species. *ACS Catal.* **2016**, *6* (4), 2473−2481.

(23) Li, J.; Chang, X.; Zhang, H.; Malkani, A. S.; Cheng, M.-j.; Xu, B.; Lu, Q. Electrokinetic and in situ spectroscopic investigations of CO electrochemical reduction on copper. *Nat. Commun.* **2021**, *12* (1), 3264.

(24) Wang, L.; Nitopi, S. A.; Bertheussen, E.; Orazov, M.; Morales-Guio, C. G.; Liu, X.; Higgins, D. C.; Chan, K.; Nørskov, J. K.; Hahn, C.; Jaramillo, T. F. Electrochemical carbon monoxide reduction on polycrystalline copper: effects of potential, pressure, and pH on selectivity toward multicarbon and oxygenated products. *ACS Catal.* **2018**, *8* (8), 7445−7454.

(25) Kastlunger, G.; Wang, L.; Govindarajan, N.; Heenen, H. H.; Ringe, S.; Jaramillo, T.; Hahn, C.; Chan, K. Using pH dependence to understand mechanisms in electrochemical CO reduction. *ACS Catal.* **2022**, *12* (8), 4344−4357.

(26) Schouten, K. J. P.; Gallent, E. P.; Koper, M. T. The influence of pH on the reduction of CO and CO_2 to hydrocarbons on copper electrodes. *J. Electroanal. Chem.* **2014**, *716*, 53−57.

(27) Moradzaman, M.; Mul, G. In situ Raman study of potential-dependent surface adsorbed carbonate, CO, OH, and C species on Cu electrodes during electrochemical reduction of CO_2. *ChemElectroChem* **2021**, *8* (8), 1478−1485.

(28) Herzog, A.; Lopez Luna, M.; Jeon, H. S.; Rettenmaier, C.; Grosse, P.; Bergmann, A.; Roldan Cuenya, B. Operando Raman spectroscopy uncovers hydroxide and CO species enhance ethanol selectivity during pulsed CO_2 electroreduction. *Nat. Commun.* **2024**, *15* (1), 3986.

(29) Zhan, C.; Dattila, F.; Rettenmaier, C.; Bergmann, A.; Kühl, S.; García-Muelas, R.; López, N.; Cuenya, B. R. Revealing the CO coverage-driven C−C coupling mechanism for electrochemical CO_2 reduction on Cu_2O nanocubes via operando Raman spectroscopy. *ACS Catal.* **2021**, *11* (13), 7694−7701.

(30) Henckel, D.; Counihan, M. J.; Holmes, H. E.; Chen, X.; Nwabara, U. O.; Verma, S.; Rodríguez-López, J.; Kenis, P. J.; Gewirth,

A. A. Potential dependence of the local pH in a CO_2 reduction electrolyzer. *ACS Catal.* **2021**, *11* (1), 255−263.
(31) Marcandalli, G.; Villalba, M.; Koper, M. T. The importance of acid−base equilibria in bicarbonate electrolytes for CO_2 electrochemical reduction and CO reoxidation studied on Au(hkl) electrodes. *Langmuir* **2021**, *37* (18), 5707−5716.
(32) Peng, H.-J.; Tang, M. T.; Halldin Stenlid, J.; Liu, X.; Abild-Pedersen, F. Trends in oxygenate/hydrocarbon selectivity for electrochemical $CO_{(2)}$ reduction to C_2 products. *Nat. Commun.* **2022**, *13* (1), 1399.
(33) Feaster, J. T.; Shi, C.; Cave, E. R.; Hatsukade, T.; Abram, D. N.; Kuhl, K. P.; Hahn, C.; Nørskov, J. K.; Jaramillo, T. F. Understanding selectivity for the electrochemical reduction of carbon dioxide to formic acid and carbon monoxide on metal electrodes. *ACS Catal.* **2017**, *7* (7), 4822−4827.
(34) Kim, J. Y. T.; Sellers, C.; Hao, S.; Senftle, T. P.; Wang, H. Different distributions of multi-carbon products in CO_2 and CO electroreduction under practical reaction conditions. *Nat. Catal.* **2023**, *6* (12), 1115−1124.
(35) You, F.; Xi, S.; Ho, J. J. Y.; Calle-Vallejo, F.; Yeo, B. S. Influence of Copper Sites with Different Coordination on the Adsorption and Electroreduction of CO_2 and CO. *ACS Catal.* **2023**, *13* (16), 11136−11143.
(36) Jouny, M.; Hutchings, G. S.; Jiao, F. Carbon monoxide electroreduction as an emerging platform for carbon utilization. *Nat. Catal.* **2019**, *2* (12), 1062−1070.
(37) Fontana, M. D.; Ben Mabrouk, K.; Kauffmann, T. H. Raman spectroscopic sensors for inorganic salts. *Royal Society of Chemistry* **2013**, *44*, 40−67.
(38) Lide, D. R. *CRC handbook of chemistry and physics*, 85th ed.; CRC Press: 2004.
(39) Persat, A.; Chambers, R. D.; Santiago, J. G. Basic principles of electrolyte chemistry for microfluidic electrokinetics. Part I: Acid−base equilibria and pH buffers. *Lab Chip* **2009**, *9* (17), 2437−2453.
(40) Wang, X.; de Araújo, J. F.; Ju, W.; Bagger, A.; Schmies, H.; Kühl, S.; Rossmeisl, J.; Strasser, P. Mechanistic reaction pathways of enhanced ethylene yields during electroreduction of CO_2−CO co-feeds on Cu and Cu-tandem electrocatalysts. *Nat. Nanotechnol.* **2019**, *14* (11), 1063−1070.
(41) Wei, P.; Gao, D.; Liu, T.; Li, H.; Sang, J.; Wang, C.; Cai, R.; Wang, G.; Bao, X. Coverage-driven selectivity switch from ethylene to acetate in high-rate CO_2/CO electrolysis. *Nat. Nanotechnol.* **2023**, *18* (3), 299−306.
(42) Gao, W.; Xu, Y.; Fu, L.; Chang, X.; Xu, B. Experimental evidence of distinct sites for CO_2-to-CO and CO conversion on Cu in the electrochemical CO_2 reduction reaction. *Nat. Catal.* **2023**, *6* (10), 885−894.
(43) Gao, J.; Bahmanpour, A.; Kröcher, O.; Zakeeruddin, S. M.; Ren, D.; Grätzel, M. Electrochemical synthesis of propylene from carbon dioxide on copper nanocrystals. *Nat. Chem.* **2023**, *15* (5), 705−713.
(44) García-Muelas, R.; López, N. Statistical learning goes beyond the d-band model providing the thermochemistry of adsorbates on transition metals. *Nat. Commun.* **2019**, *10* (1), 4687.
(45) Bai, X.; He, M.; Xu, Y.; Xu, B.; Lu, Q.; Wang, J.; Ling, C. New Mechanistic Insights into CO_2/CO Electroreduction to Acetate by Combining Computations and Experiments. *ACS Catal.* **2024**, *14* (5), 3171−3180.
(46) Kresse, G.; Furthmüller, J. Efficiency of ab-initio total energy calculations for metals and semiconductors using a plane-wave basis set. *Comput. Mater. Sci.* **1996**, *6* (1), 15−50.
(47) Kresse, G.; Furthmüller, J. Efficient iterative schemes for ab initio total-energy calculations using a plane-wave basis set. *Phys. Rev. B* **1996**, *54* (16), 11169−11186.
(48) Perdew, J. P.; Burke, K.; Ernzerhof, M. Generalized gradient approximation made simple. *Phys. Rev. Lett.* **1996**, *77* (18), 3865−3868.
(49) Grimme, S. Semiempirical GGA-type density functional constructed with a long-range dispersion correction. *J. Comput. Chem.* **2006**, *27* (15), 1787−1799.
(50) Bucko, T.; Hafner, J.; Lebègue, S.; Angyán, J. G. Improved description of the structure of molecular and layered crystals: ab initio DFT calculations with van der Waals corrections. *J. Phys. Chem. A* **2010**, *114* (43), 11814−11824.
(51) Almora-Barrios, N.; Carchini, G.; Błoński, P.; López, N. Costless derivation of dispersion coefficients for metal surfaces. *J. Chem. Theory Comput.* **2014**, *10* (11), 5002−5009.
(52) Blöchl, P. E. Projector augmented-wave method. *Phys. Rev. B* **1994**, *50* (24), 17953−17979.
(53) Kresse, G.; Joubert, D. From ultrasoft pseudopotentials to the projector augmented-wave method. *Phys. Rev. B* **1999**, *59* (3), 1758−1775.
(54) Monkhorst, H. J.; Pack, J. D. Special points for Brillouin-zone integrations. *Phys. Rev. B* **1976**, *13* (12), 5188−5192.
(55) Makov, G.; Payne, M. C. Periodic boundary conditions in ab initio calculations. *Phys. Rev. B* **1995**, *51* (7), 4014−4022.
(56) Nørskov, J. K.; Rossmeisl, J.; Logadottir, A.; Lindqvist, L.; Kitchin, J. R.; Bligaard, T.; Jonsson, H. Origin of the overpotential for oxygen reduction at a fuel-cell cathode. *J. Phys. Chem. B* **2004**, *108* (46), 17886−17892.
(57) Peterson, A. A.; Abild-Pedersen, F.; Studt, F.; Rossmeisl, J.; Nørskov, J. K. How copper catalyzes the electroreduction of carbon dioxide into hydrocarbon fuels. *Energy Environ. Sci.* **2010**, *3* (9), 1311−1315.
(58) Henkelman, G.; Uberuaga, B. P.; Jónsson, H. A climbing image nudged elastic band method for finding saddle points and minimum energy paths. *J. Chem. Phys.* **2000**, *113* (22), 9901−9904.
(59) Alvarez-Moreno, M.; de Graaf, C.; López, N.; Maseras, F.; Poblet, J. M.; Bo, C. Managing the computational chemistry big data problem: the ioChem-BD platform. *J. Chem. Inf. Model.* **2015**, *55* (1), 95−103.

https://doi.org/10.1021/jacs.4c08755
J. Am. Chem. Soc. 2024, 146, 30183−30193